Nanoscale

Surface enrichment dictates block copolymer orientation

Journal:	*Nanoscale*
Manuscript ID	NR-ART-01-2023-000095.R1
Article Type:	Paper
Date Submitted by the Author:	14-Feb-2023
Complete List of Authors:	Bae, Suwon; Brookhaven National Laboratory, Center for Functional Nanomaterials Noack, Marcus; Lawrence Berkeley National Laboratory, The Center for Advanced Mathematics for Energy Research Applications Yager, Kevin; Brookhaven National Laboratory, Center for Functional Nanomaterials

SCHOLARONE™
Manuscripts

Journal Name

ARTICLE TYPE

Cite this: DOI: 00.0000/xxxxxxxxxx

Surface enrichment dictates block copolymer orientation†

Suwon Bae,[a] Marcus M. Noack,[b] and Kevin G. Yager*[a]

Received Date
Accepted Date

DOI: 00.0000/xxxxxxxxxx

Orientation of block copolymer (BCP) morphology in thin films is critical to applications as nanostructured coatings. Despite being well-studied, the ability to control BCP orientation across all possible block constituents remains challenging. Here, we deploy coarse-grained molecular dynamics simulations to study diblock copolymer ordering in thin films, focusing on chain makeup, substrate surface energy, and surface tension disparity between the two constituent blocks. We explore the multi-dimensional parameter space of ordering using a machine-learning approach, where an autonomous loop using a Gaussian process (GP) control algorithm iteratively selects high-value simulations to compute. The GP kernel was engineered to capture known symmetries. The trained GP model serves as both a complete map of system response, and a robust means of extracting material knowledge. We demonstrate that the vertical orientation of BCP phases depends on several counter-balancing energetic contributions, including entropic and enthalpic material enrichment at interfaces, distortion of morphological objects through the film depth, and of course interfacial energies. BCP lamellae are found more resistant to these effects, and thus more robustly form vertical orientations across a broad range of conditions; while BCP cylinders are found to be highly sensitive to surface tension disparity.

1 Introduction

Block copolymer (BCP) self-assembly is a well understood process, wherein chemical incompatibility between the constituent blocks gives rise to nanoscale periodic structures.[1] The morphology that appears depends on chain architecture. For diblock copolymers (A-*b*-B), the morphology depends on chain composition (the fraction of A material, f_A); one observes the formation of lamellae (at $f_A \approx 0.5$), as well as gyroid, cylinder, and sphere nano-objects (for f_A progressively departing from 0.5).[2–5] When confined to thin films, these arrays of nano-objects can enable a host of applications, including for nanolithography,[6–9] nanowire fabrication,[10] nanoporous membranes,[11] and as coatings with tailored electrical,[12] optical,[13] and wettability[14] properties. For thin film applications, control of morphology orientation is critical. Extensive research has thus gone into directing orientation, including the use of solvent annealing,[15,16] polymer architecture,[17–21] homopolymer blending,[22,23] substrate roughness,[24] chemical patterns,[25,26] thermal gradients,[27] or thermal history.[28,29] The most direct means of influencing BCP orientation is to control the energetics of the substrate through chemical modification.[30–35] In particular, a substrate with a balanced interaction with the A and B blocks is effectively neutral, preventing preferential wetting of one block and thus promoting a vertical morphology orientation (e.g. cylinders with long axes parallel to the film normal). For instance, for polystyrene-*block*-poly(methyl methacrylate) (PS-*b*-PMMA) thin films, substrates coated with a random copolymer brush (PS-*r*-PMMA) can be used, where a brush composition of ≈ 0.5 yields vertical lamellae, while a composition of 0.3–0.4 (MMA content) is optimal for vertical cylinder phases ($f_{MMA} \approx 0.3$).[36,37]

Energetics at the free surface also play an important role in BCP orientation. For instance, PS-*b*-PMMA orients vertically most robustly when annealed close to $T \approx 225°C$, since the temperature-dependent surface tensions of PS and PMMA cross at this temperature, eliminating the preference for one block to cover the free surface (which would reorient the morphology to be horizontal).[38–40] One can generally expect that BCP materials with extremely different surface tensions (between the two blocks) will be difficult to order vertically, whereas materials with small surface tension differences should readily form vertical morphologies. Correspondingly, the differences in self-assembly behavior observed for the many different BCP materials that have been studied (which include PS-*b*-

[a] Center for Functional Nanomaterials, Brookhaven National Laboratory, Upton, New York 11973, USA. E-mail: kyager@bnl.gov
[b] The Center for Advanced Mathematics for Energy Research Applications, Lawrence Berkeley National Laboratory, Berkeley, California 94720, USA.

† Electronic Supplementary Information (ESI) available: Supporting documentation includes visualization of vertical fraction calculation, definition of GP kernel, distribution of simulation data-points, and additional examples of morphological snapshots and slices through the model space. See DOI: 00.0000/00000000.

PMMA,[37,41] PS-*b*-polyvinylpyridine,[42] PS-*b*-polyisoprene,[43] and PS-*b*-poly(dimethyl siloxane)[21,44,45]) must be due in part to the different surface tensions. Despite the importance of surface tension disparity to BCP ordering, this property has not been studied as carefully as other aspects of BCP thin films (such as segregation strength and substrate energy). This may be due in part to the difficulty in experimentally varying surface tension in a systematic way, without also modifying countless other material properties.

Molecular dynamics (MD) simulation, a common approach for studying the behavior of polymers,[46–48] has been used with great success to capture the ordering of BCP morphologies.[49–52] Coarse-grained models allow one to probe fundamental ordering phenomena, and uncover trends that are not tied to any particular monomer chemistry. Here, we use coarse-grained MD simulations to study the ordering and orientation of BCP thin films, exploring the interplay between chain composition (f_A), surface tension disparity (α), and substrate energy (Γ). By using an abstracted (coarse-grained) model, we uncover the fundamental way in which surface tension controls ordering, and in particular elucidate why opposite-tone materials (f_A vs. $1-f_A$) are not equivalent. Since the model retains the notion of individual chains, we are able to directly interrogate the polymer conformation and chain distribution, and better understand energetic tradeoffs.

Exploring the proposed multi-dimensional parameter space could be challenging, especially considering the computational cost of MD simulations. Exhaustive grid searches in high-dimensional spaces are generally inefficient, as resources (in this case, computational) are wasted measuring nearly-identical systems, while areas of interest in the space (where behavior changes rapidly) may be under-sampled. Naive search methods do not take into account the complex interplay between parameters caused by the underlying physics. In the case of BCPs, a plethora of inter-related parameters influence ordering.[30,53–55] In this study, we deploy an autonomous experimentation (AE) paradigm based on Gaussian process (GP) modeling to efficiently select points in the parameter space for study.[56] An autonomous loop iteratively selects new simulations to perform based on the structure of the evolving dataset. The underlying GP model is designed to capture known symmetries of the problem, and as it progressively retrains on accumulating data, provides increasingly robust predictions for high-value portions of the parameter space to investigate. GP automation of the exploration improves search efficiency, while also yielding a final robust physical model for the entire space (effectively interpolating and extrapolating the available data).

2 Results and Discussion

To explore morphology orientation in BCP thin films, we deployed coarse-grained bead-spring molecular dynamics to simulate diblock copolymer (A-*b*-B) chains.[57] The initial state is a disordered film sitting on a substrate, wherein the constituent chains are mixed and randomly configured. Simulation consists of allowing thermal annealing to proceed, wherein the blocks phase separate locally, the chains self-assembly into a morphology, and the morphology reorganizes into a preferred orientation. We explore the three-dimensional (3D) parameter space of chain composition, surface tension disparity, and substrate surface energy (f_A, α, Γ). We conduct MD simulations at select points within the space, compute structural metrics of interest (especially evaluating the vertical fraction of the morphology, f_V), and combine all data into a predictive model for the entire space using Gaussian process methods. We adopted an autonomous data acquisition strategy (refer to Methods for details), by automating the preparation and execution of MD simulations, analysis of resultant morphological structures, construction of GP model, and selection of subsequent simulation points. Selection of new points exploits the GP model, and uses an objective function that balances between information gain (minimizing uncertainty so as to explore the space) and focusing data in the transition region between vertical and non-vertical ordering (by targeting $f_V \approx 0.8$ in the GP surrogate model). This machine-learning procedure for exploration and modeling efficiently reconstructs the physical behavior in the parameter space.

We begin by considering canonical vertical ordering of cylindrical and lamellar BCPs (Figure 1). Consistent with experiment,[36,37] one observes a range of surface energy (Γ) for which a given morphology is predominantly vertical (high vertical fraction). The substrate is expected to be neutral when it establishes balanced energetic contributions with the A and B blocks, when accounting for the relative concentration of these two bead types. A neutral substrate prevents preferential wetting of one block at the substrate, and thereby allows a vertical morphology (where both blocks are in contact with the substrate) to arise. For lamellae ($f_A = 0.5$) this vertical window is symmetric and centered about $\Gamma = 0.5$. For cylinder-forming material, this window is narrower, and shifted to smaller Γ. This is due to the different material composition, $f_A = 0.25$, but it is noteworthy that the center of this vertical window does not coincide with the nominal composition. Our method for computing vertical fraction relies on the projected maps of A and B material (refer to Methods and ESI Figure S2), and is thus sensitive to both orientational disorder and fluctuations of the A/B interblock interface. Even clearly vertical morphologies (such as examples in Figure 1) will yield vertical fraction somewhat less than 1.0. Nevertheless, it is evidently harder to orient cylinder materials vertically, as they are less tolerant to variations in Γ. The asymmetric shape of the cylinder vertical window suggests additional parameters beyond Γ play a role in controlling structure formation. Observations such as these motivate a more thorough investigation of the underlying balance of forces that dictate whether a BCP orders vertically.

When considering the full 3D parameter space defined by chain composition, surface tension disparity, and substrate energy, a number of different kinds of behavior are observed (Figure 2). As expected, there is a sharp phase boundary between the formation of cylinder phases and lamellar phases (the latter appears for $0.35 \leq f_A \leq 0.65$). There is a broad region of intermediate surface energy for which one observes well-ordered vertical morphologies (e.g. Figure 1a & b, Figure 2b & d), whereas for highly preferential substrates one instead observes horizontal morphologies (in-plane cylinders or lamellae layering in z direction). These horizontal states may be accompanied by the formation of islands

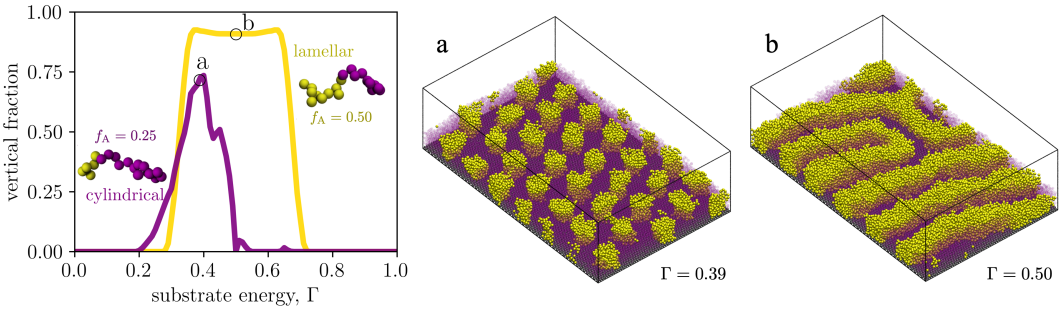

Fig. 1 Orientation of block copolymer morphologies in thin films depends strongly on the substrate's surface energy. (left) Cylindrical ($f_A = 0.25$, purple curve) and lamellar ($f_A = 0.5$, yellow curve) morphologies orient vertically across a small range of substrate energy (Γ). The vertical window for cylinder materials is shifted towards smaller Γ, consistent with chain composition, and is narrower (results are shown for materials with no surface tension disparity, $\alpha = 0$). Representative molecular dynamics snapshots for (a) cylinder and (b) lamellar materials are shown, where the minority block A beads are depicted yellow, while the majority block B beads are purple and slightly transparent.

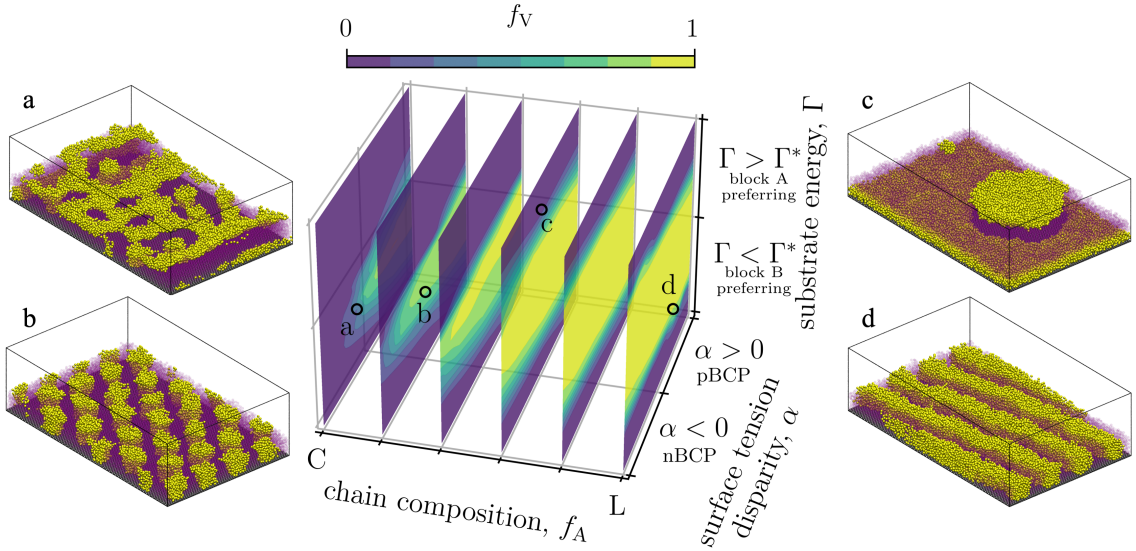

Fig. 2 Morphology orientation (vertical fraction, f_V, depicted using the color scale shown above) is studied throughout a three-dimensional parameter space defined by chain composition, surface tension disparity, and substrate energy. Select MD simulation results from the space are depicted (a–d); refer to ESI Figures S3–S10 for additional snapshots. The full 3D model is built using Gaussian process methods. Chain composition is varied from asymmetric cylinder chains ($f_A = 0.25$, C) to symmetric lamellar chains ($f_A = 0.50$, L). Surface tension disparity (α) describes the difference in self-cohesion of the two blocks; $\alpha = 0$ yields a material where both blocks have the same surface tension, $\alpha > 0$ indicates that the minority block has higher surface tension (we refer to these as pBCP materials), and $\alpha < 0$ indicates majority has larger surface tension (nBCP). Substrate energy is defined to be consistent with the corresponding composition of a random copolymer brush, where $\Gamma < \Gamma^*$ exhibits preferential interaction with the majority B beads.

or holes on the free surface, to accommodate layering within an incommensurate thickness (Figure 2c).[58–60] At the boundary of vertical ordering in the parameter space, one observes mixed orientations and defective states (Figure 2a). The 3D space exhibits known symmetries, which were embedded in the GP kernel to improve model fidelity. In particular, ordering at (f_A, α, Γ) is necessarily identical at $(1-f_A, -\alpha, 1-\Gamma)$, since a given BCP material composition (f_A) and its opposite ($1-f_A$) are the same material, as long as one exchanges the energetics of the blocks.[1] This point symmetry can be easily seen in the $f_A = 0.5$ slice (Figure 3). It also allows us to focus on $f_A \leq 0.5$ without loss of information.

The trend as a function of surface tension bears particular scrutiny. We define surface tension disparity (α) such that $\alpha = 0$ indicates the two blocks have identical surface tension, $\alpha > 0$ indicates that the A (minority) material has larger surface tension (we refer to these positive α materials as pBCP), and $\alpha < 0$ thus refers to materials where the B (majority) material has larger surface (we refer to these as nBCP). For real BCP materials, α is determined by the selection of monomers for the two polymer blocks. Both pBCP and nBCP materials are investigated experimentally, with the former being more common. For instance, PS-*b*-PMMA cylinders where the PMMA is the minority is pBCP (at typical annealing temmperatures $T < 220°$), whereas the opposite-tone material (PMMA majority) would be nBCP (the corresponding morphology is referred to as inverse cylinders).[9]

Obviously for perfectly symmetric BCP chains ($f_A = 0.5$), the sign of α does not matter, and the space is correspondingly symmetric. The vertical window for lamellae is centered about $\Gamma = \Gamma^*$, since this is where the substrate interaction strength is identical for both bead types. The window is wide, and remains so for a broad span of α values (Figure 4, bottom). The robust vertical ordering of lamellae is consistent with entropic arguments for the vertical state being intrinsically more stable due to chain entropy at interfaces (i.e. vertical is the preferred orientation when surface enthalpy does not play a role).[34] When looking beyond symmetric lamellae ($f_A \neq 0.5$), what is immediately striking about the trend with α is the strong asymmetry (Figure 3). At first, one might assume that if a particular BCP material forms vertical morphology, then the opposite material ($1-f_A$) will also form a vertical state (as long as one selects the right surface energy). However, we find that it is much harder to form vertical morphologies for nBCPs (narrow or non-existent vertical window) than the corresponding pBCPs (Figure 4, top). This asymmetry becomes more pronounced for larger $|\alpha|$ (ESI Figures S11 and S12).

This behavior can be understood based on the relative volume fractions of materials expressed at the free surface. For pBCP vertical cylinders, a relatively small surface area of high surface tension minority material must be exposed at the free surface. For nBCP cylinders, the majority (matrix) material is the high surface tension component. Presenting a large surface area of high-energy material naturally destabilizes this configuration. Thus, simple volume fraction arguments explain the general phenomena of nBCP materials being difficult to orient vertically. However, in both pBCP and nBCP cases, the ordering energetics could be complicated by reorganization of the constituent BCP chains; one would expect some local rearrangement of chains in order to minimize the amount of high surface tension material exposed at the free surface. To probe this, we compute the density of minority A material through the film depth (Figure 5). This data clearly shows a depletion of A beads at the film surface for pBCPs, with the extent of depletion scaling with α. One correspondingly observes an increase in A beads in the interior of the film. Cross-sections through the film confirm that this reorganization in chains corresponds to a bulging of the morphological objects (Figure 5 and ESI Figure S14), with vertical cylinders distorting into shapes with larger midsection that taper towards interfaces. The effect is less pronounced for lamellae, but here again one observes bulging near the film midplane for larger α (Figure 5c & d). In the opposite regime of nBCP, one correspondingly observes a small enrichment of minority beads at the free surface, and associated depletion from the film interior. The distortion of morphological objects away from the bulk equilibrium shape necessarily incurs an energy penalty. In order to maintain the vertical orientation, this distortion energy must be sufficiently compensated by other terms in the energy balance, especially the overall chain entropy preference for vertical orientation,[34] and a favorable substrate interaction.

Another important effect that could lead to chain enrichment at interfaces is entropic segregation. Shorter polymer chains are driven to interfaces, since the corresponding entropy loss is smaller.[61] For asymmetric BCP chains, this could cause the shorter chain end (minority beads) to accumulate near interfaces.[62] To probe this question, we consider the portion of the parameter space where enthalpic effects are minimized, and thus entropic effects dominate. The $\alpha = 0$ slice (Figure 6) eliminates disparity in the surface tension terms, and the associated interfacial enrichment effects. Tracking the center of the vertical window (Figure 6c) follows the conditions where substrate interaction energies are balanced. In this regime, one observes a distinct enrichment of minority beads at the free surface, as f_A becomes smaller, supporting the hypothesis of entropic enrichment of the minority component. This is consistent with prior work showing that BCP chain architecture affects the entropic contribution to orientation.[17,19–21]

The position of the vertical window can now be rationalized. To a first approximation, one might expect the vertical window to follow $\Gamma \approx \Gamma^*$, since this is where the interaction with the substrate is identical for both bead types. While the neutral window is indeed centered around Γ^* for lamellae ($f_A = 0.5$), it deviates strongly from this trendline for other chain compositions. Indeed, for decreasing f_A along $\Gamma = \Gamma^*$ one observes a conversion to horizontal orientation (as can be seen by layering of the density profile, Figure 6b). Of course, the shifting of the vertical window to smaller Γ for smaller f_A is a consequence of the relative concentration of bead types at the substrate interface. With a larger fraction of B beads, the energy balance can be improved by shifting to smaller Γ (emphasizing the contribution of a stronger B-substrate interaction term). Based on this argument, one might expect the vertical window to follow $\Gamma \approx \Gamma^* + (f_A - 0.5)$. However, this expectation does not take into account the effects noted above. Thus, the actual position of the neutral window—$\Gamma \approx \Gamma^* + 0.5(f_A - 0.5)$—is due to the local con-

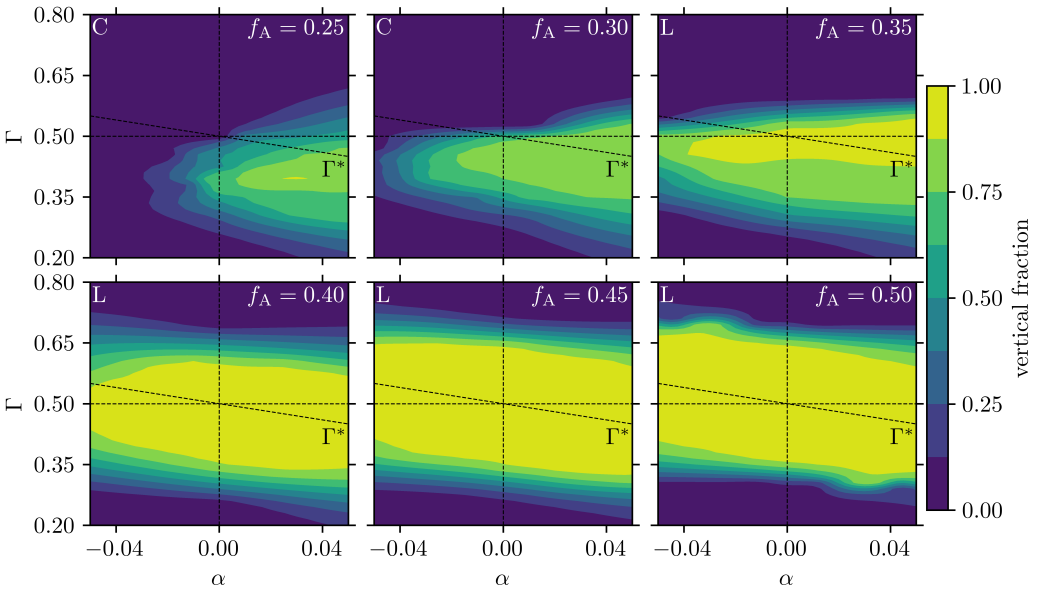

Fig. 3 Select slices through the Gaussian process (GP) model describing morphology orientation. The dashed line denotes where the substrate exhibits no block preference (Γ^*). The window of vertical orientation (yellow) is broad and centered around Γ^* for symmetric (lamellar) BCPs. For asymmetric chains, the window narrows and shifts away from Γ^*; it is in general more difficult to form vertical morphologies for cylinder phases. Surface tension disparity plays a major role in orientation behavior. Of particular note is the dissimilarity between pBCP and nBCP cylinders, despite them being simple inverses of each other when considered structurally. It is difficult to generate a stable vertical orientation of nBCPs since this requires exposing a large area of high surface-tension matrix material at the film-vacuum interface.

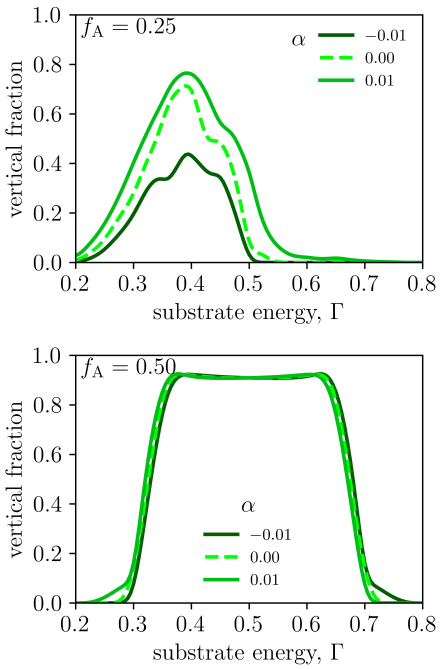

Fig. 4 Different ordering is observed for pBCP and nBCP. For lamellar materials ($f_A = 0.50$), pBCP and nBCP materials are conceptually equivalent, and thus exhibit the same vertical window. For asymmetric chains, nBCP ($\alpha < 0$) materials have a large surface tension associated with the matrix material. This disfavors the vertical orientation, resulting in a narrow window and lower vertical fraction. It is conversely much easier to generate vertical orientations for pBCP materials. (Refer to ESI Figure S11 for other f_A.)

centration at the substrate (nominal chain composition and local enrichment), as well as the energy penalty of the distorted morphologies that arise for vertical orientation under the given conditions.

To emphasize this point, consider the ordering of $f_A = 0.25$ cylinder chains ($\alpha = 0$) on a $\Gamma = \Gamma^*$ substrate. Although it is obvious that such a material exhibits a stronger interaction with a $\Gamma \approx 0.3$ substrate, it is at first unexpected that it cannot also form a vertical orientation at Γ^*. After all, the bead-substrate interactions are equal, and the bead interactions at the free surface are also equal. There is thus no enthalpic gain associated with switching from vertical to horizontal morphology, or otherwise changing the bead composition at the interfaces; and so the vertical state should be accessible. However, such an analysis omits the distorted shape of vertical objects (due to local enrichment), which induces an energy penalty that must be compensated through sufficiently strong substrate interactions. In this sense, substrate neutrality is not sufficient; the substrate must moreover interact strongly enough with both blocks to compensate for the energy penalties of the vertical orientation. Moving away from the $\alpha = 0$ slice then requires inclusion of the additional effect of enthalpic enrichment/depletion at interfaces, which further distorts the shape of objects.

There are notable differences between the cylinder-forming materials (C chains) and lamellae-forming materials (L chains). The C materials seem more sensitive to interface conditions, exhibiting a narrower vertical window and strong dependence on α, while L materials robustly form a wide vertical window across a broad range of conditions. These trends can be understood by considering differences at multiple scales. At the scale of individ-

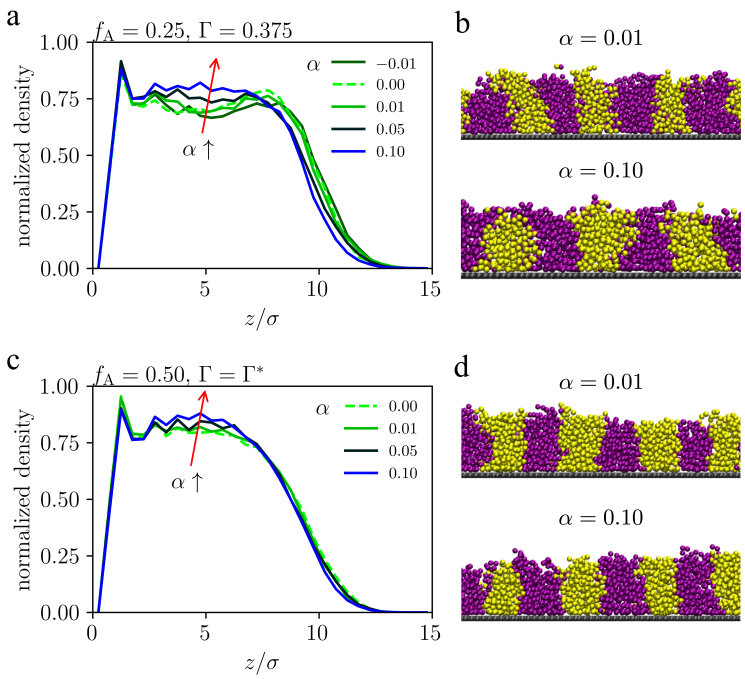

Fig. 5 Surface tension disparity (α) affects the precise shape of morphological objects, which can be seen in the average density of minority A beads (normalized by f_A) through the film thickness (a, c) and representative simulation cross-sections (b, d). Results are shown for neutral substrates, at $T = 1.2\varepsilon/k_B$ (before final equilibration at $T = 0.8\varepsilon/k_B$). As the surface tension of the minority A block becomes larger (α increasing, red arrow), more B material is expressed at the surface, causing vertical cylinders to bulge within the film interior (a, b). The nBCP material ($\alpha = -0.01$) conversely concentrates more minority beads at the surface in order to displace the higher surface tension matrix beads. Vertical lamellae exhibit the same effect, though less starkly (c, d). Additional cross-sectional images are available in ESI Figure S14.

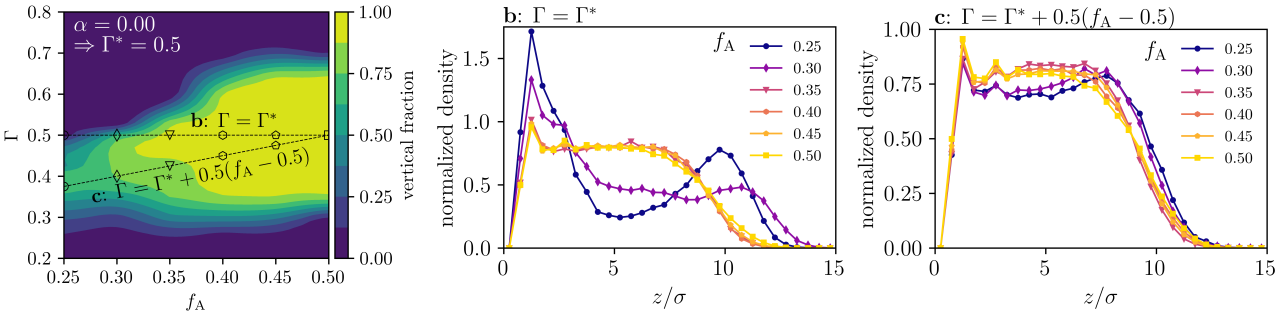

Fig. 6 (left) A representative slice through the model space (at $\alpha = 0$) demonstrates how chain composition (f_A) has a strong effect on orientation behavior. (b) Normalized film density profiles along the thickness direction (z) for the minority A beads, for select simulations at $\Gamma = \Gamma^*$ (at $T = 1.2\varepsilon/k_B$). (c) Density profiles along a trendline that follows the center of the vertical orientation window (at $T = 1.2\varepsilon/k_B$). Of note is that the window of vertical orientation does not follow the Γ^* trendline (b), despite this being the condition where substrate-bead interaction strengths are matched for majority and minority blocks. The corresponding density shows the signature of horizontal morphologies (layering along z) for $f_A < 0.35$. The center of the neutral window (c) is offset towards smaller Γ due to local composition at the substrate interface, which is influenced by f_A as well as entropic-driven enrichment of shorter chain-ends (as can be seen in the density profiles, and corresponding MD snapshots in ESI Figure S13).

ual chains, L chains are symmetric (or near-symmetric). Thus, the competing interactions associated with the two blocks are inherently close to balanced. The more asymmetric C chains have unbalanced energetic contributions, which must be compensated for (e.g. by carefully tuning Γ). At the scale of the morphological interface, lamellae exhibit zero-curvature flat interfaces, while cylinders are curved nano-objects. While BCP lamellae can curve over large lengthscales, local distortions in flat lamellae sheets incur a large energy penalty. By comparison, locally distorting a cylinder object in some sense amounts to merely redistributing existing interfacial curvature. We correspondingly observe more α-induced bulging of cylinders than lamellae (Figure 5). At the scale of the morphology, the formation of mixed orientation states (coexistence of horizontal and vertical grains) for L materials involves the creation of a high-energy defect boundary in between the two orientations. The abutment of the two orientations involves either a termination of lamellar sheets or continuous twisting of lamellae orientation; both options incur significant bending energy penalties. By comparison, the boundary between a horizontal and vertical domain for cylinder phases can be easily accommodated. The majority matrix forms a continuous domain, and thus simple rearrangement of B chain ends in the majority can accommodate such a boundary. This explains the relatively abrupt transition between vertical and horizontal regions in the parameter space for L chains, as compared to the continuous transition observed for defect-tolerant C chains. Combined, these differences at various scales (chain, interface, morphology) explain the significant ordering differences observed across the full parameter space (Figure 2 and Figure 3).

These considerations explain the breadth of the vertical region for L chains in both the Γ and α directions. The resistance of the lamellar morphology to distortion causes this system to suppress enrichment at interfaces; the smaller distortion energy penalty correspondingly broadens the range of enthalpic conditions suitable for vertical orientation.

As we have seen, the surface tension disparity (α) plays an important role in determining the orientation of a BCP morphology, by setting the energetic contribution of interfaces, affecting chain enrichment, and thereby influencing morphology shape. In the nBCP regime, α essentially destabilizes the vertical morphology, by making it highly unfavorable for the majority matrix material to be present at the film surface. In the pBCP regime, α can correspondingly be thought of as stabilizing the vertical orientation; the width of the vertical region increases with increasing α. This occurs because of the lower surface energy associated with the majority component; the total interfacial energy is further lowered by depletion of the high-energy minority component. Increasing α for pBCP is similar to adopting a B-preferential substrate (smaller Γ) since both of these effects serve to drive majority B beads to the interface. Of course, the vertical orientation cannot be stable to arbitrarily large α, since increasing α is also distorting the morphology, and increasing the enthalpic penalty for the small amount of A beads at the interface. At sufficiently large α, we observe complete wetting of the surface by the majority beads, and corresponding disruption of the entire morphology (ESI Figures S14 and S15).

The results presented here have focused on the BCP monolayer regime, where the film thickness is somewhat less than the morphology repeat spacing. It is known experimentally that achieving uniform vertical orientation through the entire thickness of the film becomes more challenging as film thickness increases,[63] since preferential orientation at interfaces must be sufficiently strong to propagate through the film interior. We expect that the effects described here are operative also in thicker films. That is, enthalpic and entropic effects will continue to drive chain enrichment/depletion at interfaces, which will correspondingly alter the relative energy of local vertical or horizontal orientation (ESI Figures S16 & S17). However, propagation of orientation will be hindered by competition with ordering in the film interior (which will tend to initially phase-separate into a random orientation).

3 Conclusions

We carried out MD simulations of BCP thin films using a coarse-grained model, and exploited a machine-learning autonomous strategy to efficiently explore morphological ordering and orientation. The final GP model, designed with physics constraints (known energetic symmetries) and trained on the full set of simulations, represents a robust predictive model for BCP orientation in thin films.

Using this system-agnostic model, we uncover the dominant effects that dictate orientation in BCP films. Absent enthalpic effects, configurational entropy at surfaces drive BCP phases to adopt a vertical orientation. Substrate surface energy then competes with this intrinsic behavior, reorienting the morphology to be horizontal if the substrate is sufficiently preferential for one of the blocks. Surface tension disparity modulates this tradeoff, increasing the enthalpic cost for the vertical orientation if the majority component is higher surface tension. Both surface tension disparity and chain entropy can drive enrichment or depletion of one of the blocks at interfaces; this changes the shape of the morphological object through the film depth. These morphological distortions have corresponding energy penalties, which must be counter-balanced by sufficiently strong substrate interactions in order for the vertical state to be favorable. All of these effects contribute to the total energy balance, which regulates whether the vertical or horizontal orientation is more stable.

These effects are all more extreme for asymmetric BCP chains (i.e. cylinder-forming material) than for symmetric BCPs (lamellae-forming). In particular, lamellae-forming materials have more balanced energetic contributions (owing to similar mass fractions for the two blocks), have more rigid morphologies that resist distortion (flat lamellar interfaces), and are less tolerant to orientational boundaries (morphologies more uniform).

This enhanced understanding of BCP ordering should enable prescriptive tuning of orientation, through molecular design (e.g. selecting surface tension disparity) and ordering conditions, including substrate energy and annealing temperature (which influences surface tensions). Since orientation is critical to applications of BCP thin films as nanostructured coatings, this work should enable enhanced material design. Moreover, the presented strategy for combining machine-learning exploration and modeling with a generalizable molecular simulation is extendable to a

great many problems in self-assembling materials. This strategy is thus promising for improved efficiency in material discovery.

4 Methods

4.1 Chain definition and film configuration

We simulate diblock copolymer chains, A-*b*-B, using a bead-spring model (Kremer-Grest),[46] with previously-validated parameters.[57] BCP can be simulated using purely repulsive interactions, where confinement between parallel plates is used to enforce thin film behavior.[64–66] However, such a configuration does not naturally capture the full range of phenomena associated with a free polymer-vacuum interface, such as surface restructuring into islands and holes.[34,67] Such simulations make it impossible to study the role of free surface tension. We instead use a model with attractive potentials (bead-bead and bead-substrate) so that cohesion consolidates the polymer chains into a film adhered to the substrate with a free surface.[34,57]

The chain length is set to $N = 20$ beads for all chain compositions, f_A. We follow a convention where the A beads are the minority phase ($f_A < 0.5$) and thus B forms the majority matrix; of course for symmetric lamellar chains ($f_A = 0.5$) this distinction does not exist. Blocks A and B are constructed by beads of the corresponding type, where every beads has unit mass ($1m$). Lennard-Jones (LJ) units are used, where σ, ε, and $\tau = \sigma(m/\varepsilon)^{1/2}$ are units for length, energy, and time, respectively. A thin film is simulated using 1800 BCP chains, resulting in the film thickness of $h < L_0$ where L_0 is the domain/repeat spacing of lamellae and cylinders. The interactions between constituent beads are governed by a finitely extensible nonlinear elastic (FENE) potential for bonded interactions (Equation 1) and a Lennard-Jones (LJ) potential for non-bonded interactions (Equation 2). The simulation box has in-plane periodic boundary conditions and a size of $L_x = 57\sigma$ and $L_y = 90\sigma$; in the out-of-plane direction the box height L_z is set to be larger than the BCP film thickness (h), such that the system naturally forms a free surface (polymer-vacuum interface). The initial configuration of each film is a disordered state, where the constituent chains exhibit no phase separation, and is generated using a self-avoiding random walk algorithm. Individual films are placed on top of a substrate whose constituent beads (type S) interact with chain beads with non-bonded interactions described by another LJ potential. The substrate is a layer of hexagonally packed beads of type S, which are immobile and interact only with BCP chain beads in a pairwise manner. In Equations 1 and 2, k is a spring constant, R_0 is a maximum length, and ε_{ij} and σ_{ij} are the interaction strength and the zero-crossing distance between a bead of type i and another of type j. The ε_{AA} and ε_{BB} interaction parameters account for self-cohesion energies of A and B beads, and thus capture the surface tension of each block. The ε_{AB} parameter accounts for the interaction between the two blocks; since this interaction is set to be weaker than either of the self-cohesion terms, there is a net drive towards phase-separation (ε_{AB} thus sets the segregation strength, c.f. the Flory-Huggins parameter χ). The ε_{SA} and ε_{SB} parameters are the interaction strengths between the chain and substrate beads and thus determines the substrate interfacial energy. These ε parameters as well as f_A are responsible for the ordering of the corresponding BCP films. The other parameters for the potentials are constants and given in Table 1. Note that the LJ part of the FENE potential is cut off at $2^{1/6}\sigma_{ij}$ and purely repulsive, while the LJ potential responsible for non-bonded interactions is cut off at $r = 2.5\sigma_{ij}$ in order to make take into account attractive interactions as well as repulsive ones.

$$U_{\mathrm{FENE}}(r) = -0.5kR_0{}^2 \ln\left[1-\left(\frac{r}{R_0}\right)^2\right] + 4\varepsilon_{ij}\left[\left(\frac{\sigma_{ij}}{r}\right)^{12} - \left(\frac{\sigma_{ij}}{r}\right)^{6} + C_1\right] \quad (1)$$

$$U_{\mathrm{LJ}}(r) = 4\varepsilon_{ij}\left[\left(\frac{\sigma_{ij}}{r}\right)^{12} - \left(\frac{\sigma_{ij}}{r}\right)^{6} + C_2\right] \quad (2)$$

4.2 Parameter space

To study the orientation of BCPs, we systematically explore three parameters that are critical to ordering in thin films: BCP chain composition (f_A), surface tension disparity between the two blocks (α), and substrate interfacial energy (Γ). Chain composition is defined based on the fraction of chain beads that are type A; we explore from $f_A = 5/20 = 0.25$ (cylinder-forming chains) to $f_A = 10/20 = 0.50$ (symmetric chains that form lamellae). Since the BCP chain length is fixed at $N = 20$, the increment of f_A is $1/20 = 0.05$.

We define the parameter α so that it quantifies the disparity between the surface tension of the two blocks; as shown in Equations 3 and 4, the parameter modifies the self-cohesion terms ε_{AA} and ε_{BB}. For $\alpha = 0$, the two blocks have identical surface tension ($\varepsilon_{AA} = \varepsilon_{BB}$) and there is thus no enthalpic preference for which block is present at the free surface. Although such a material might be difficult to realize experimentally, it acts as a crucial control. Positive α corresponds to BCP chains with $\varepsilon_{AA} > \varepsilon_{BB}$, where the minority component (e.g. cylinder cores) has a higher surface tension than the majority matrix. We refer to such materials as "pBCP," and note that many of the experimentally-studied BCPs are of this type. For instance, most experimental reports for cylinder-forming polystyrene-*block*-poly(methyl methacrylate) are for the material where polystyrene (which has lower surface tension) forms the matrix. We denote negative α BCP chains as "nBCP" ($\varepsilon_{BB} > \varepsilon_{AA}$), where the majority matrix material has a higher surface tension. The larger the magnitude of α, the larger the difference in self-cohesion energies between the blocks. To understand the scale of α, we note that for a typical experimental BCP (such as PS-*b*-PMMA) at typical annealing temperatures, one would estimate $\alpha \approx 0.007$.

$$\varepsilon_{AA} = (1+\alpha)\varepsilon \quad (3)$$

$$\varepsilon_{BB} = (1-\alpha)\varepsilon \quad (4)$$

The parameter Γ is used to define the substrate interaction,

Table 1 Parameters of potentials used to described interactions between beads.

k	R_0	ε_{AB}	σ_{AA}	σ_{BB}	σ_{AB}	σ_{SA}	σ_{SB}	C_1	C_2
$30\varepsilon/\sigma^2$	1.5σ	0.5ε	1.0σ	1.0σ	1.0σ	1.0σ	1.0σ	0.25	$(2/5)^6(1-(2/5)^6)$

where small values ($\Gamma \approx 0$) yield a substrate with a strong preference for the majority B beads, and large values ($\Gamma \approx 1$) yield a substrate preferential for the minority A beads. This behavior is constructed by computing the film-substrate interaction terms ε_{SA} and ε_{SB} using Γ, and also ε_{AA} and ε_{BB} (Equations 5 and 6) in a linear relationship (see ESI Figure S1). Conceptually, these definitions model the experimental case of a substrate chemically modified with random copolymer brush. That is, Γ can be thought of as the composition of the random copolymer, or, more specifically, as the relative fraction of A-type monomer units forming the substrate.

$$\varepsilon_{SA} = (1-\Gamma)\varepsilon_{AB} + \Gamma\varepsilon_{AA} \tag{5}$$

$$\varepsilon_{SB} = \Gamma\varepsilon_{AB} + (1-\Gamma)\varepsilon_{BB} \tag{6}$$

Note that ε_{SA} and ε_{SB} are dependent on α (in addition to Γ) since α alters ε_{AA} and ε_{BB}, which are the limiting values at $\Gamma =$ 0 and 1. To assist in reasoning about substrate conditions, we define Γ^* as the Γ for which $\varepsilon_{SA} = \varepsilon_{SB}$ (Equation 7). In principle, Γ^* is thus a neutral substrate (equal interaction with both bead types). The substrate is A block preferential for $\Gamma > \Gamma^*$ and B block preferential for $\Gamma < \Gamma^*$.

$$\Gamma^* = 0.5\,[1 - \alpha/(\varepsilon - \varepsilon_{AB})] \tag{7}$$

4.3 Molecular dynamics simulations

We utilized the large scale atomistic/molecular massively parallel simulator (LAMMPS) made available by Sandia National Laboratory and the Institutional Cluster of the Scientific Data Computing Center at Brookhaven National Laboratory to carry out molecular dynamics simulations.[68] In order to make BCP chains in a simulation box represent a thin film, periodic boundary conditions were imposed along the x and y axes. Every BCP film was equilibrated at $T = 1.2\varepsilon/k_B$ for at least $t = 240{,}000\tau$, followed by another equilibration at $T = 0.8\varepsilon/k_B$ for $t = 60{,}000\tau$ with the NVT ensemble and a Nosé-Hoover thermostat adopted for both equilibrations (k_B is the Boltzmann constant). Presented results are after the conclusion of the $T = 0.8\varepsilon/k_B$ equilibration, unless otherwise specified. Molecular snapshots were generated by using the visual molecular dynamics (VMD) software package.[69]

4.4 Characterization of morphologies

The morphology of each BCP thin film was characterized primarily by the vertical fraction (f_V), the fraction of the morphology within the simulation that is oriented vertically as opposed to horizontally or randomly. For BCP cylinders, the vertical orientation is that for which the cylinder long-axis is out-of-plane; while for lamellae, the vertical orientation is when the lamellar normal is in-plane (sheets are out-of-plane). In both cases, the vertical orientation is the configuration expected on neutral surfaces, where both blocks are in contact with the substrate. We calculate f_V by assessing the areal fraction of minority component material that projects through the entire film thickness. In particular:

$$f_V = \frac{\sum_{xy}\left(A(x,y) \cap B(x,y)^C\right)/(L_x L_y)}{f_A} \tag{8}$$

where $A(x,y)$ and $B(x,y)$ represent maps of A and B material (projection along z), the superscript C denotes the complement operation, $\cap$ is the intersection operation, and the sum is over the x and y spatial coordinates. Thus, we intersect a spatial map of the minority A material (i.e. all locations with some A) with the complement of the majority B material (all locations without any B) to yield a map of vertical structures (all locations where only A appears). This summed area is normalized by the box size and by composition (to account for the maximum possible sum that would be measured when all material is vertically aligned). Refer to ESI Figure S2 for visualizations. This normalized definition of f_V is universal in the sense that it ranges a minimum value of 0 to a maximum 1, for all f_A.

This definition of f_V quantifies orientation, yielding $f_V = 0$ for completely horizontal morphologies, and $f_V = 1$ for perfectly vertical. Nominally vertical morphologies with some tilt will decrease the value of f_V through this projected calculation. However, it is also true that roughness in a nominally vertical morphology will decrease the computed f_V; thus this metric is sensitive to orientational disorder and also interfacial disorder. This interfacial effect is more pronounced in vertical cylinders than in vertical lamellae, which results in systematically lower values for the the maximum f_V for cylinder phases.

4.5 Autonomous exploration of the parameter space

In order to efficiently explore and model the defined parameter space, we deployed an autonomous experimentation (AE) paradigm based on Gaussian process (GP) modeling.[56,70–72] In this case, each experiment consists of launching an MD simulation. The GP model posterior mean of the defined 3D parameter space is denoted $M(f_A, \alpha, \Gamma)$; each combination of f_A, α, and Γ yields a particular morphology, which is characterized by vertical fraction (f_V). The GP modeling computes a posterior mean, which is a Bayesian prediction of f_V throughout the space. The AE loop consists of 1) running an MD simulations for a particular point in the parameter space, 2) automatically analyzing the morphology to extract structural metrics (especially vertical fraction), 3) updating the parameter space GP model M, and 4) selecting the next simulation point based on M. The AE approach iteratively and autonomously selects new points for simulation, and thus naturally fills in the space with data, progressively improving the quality of the model. The selection of points (i.e. the AE objective function) is based on Gaussian process regression (described below) and optimized to identify the boundary of the

vertical region while minimizing model error. We manually selected an initial set of simulation points during exploration of the MD model; these simulations were used as initialization for the AE. The resultant final trained model $M(f_A, \alpha, \Gamma)$ is the posterior mean of a Gaussian process regression carried out using all measurements (359 simulations, placement shown in ESI Figure S3); it is this optimized model that is visualized throughout the main text.

4.6 Gaussian process regression

We used Gaussian process regression (GPR) to obtain a three-dimensional model (M) describing the orientation map, and also to enable autonomous data acquisition and parameter space exploration.[56] GPR is a non-parametric, statistical method used to approximate a function value and quantify uncertainty. It does not require one to specify the architecture of the model function beforehand; the model grows more sophisticated as more data is accumulated. A GP uses kernel/covariance functions, which can be interpreted as the similarity between pairs of collected data points. All functions in the function space underlying a GP are weighted sums of the kernel function whose exact shape depends on so-called hyperparameters. For our kernel definition, the primary hyperparameters (associated with each axis of the parameter space) can be interpreted as correlation lengths (refer to ESI Figure S3 for best-fit values). Using the trained hyperparameters, the kernel describes the similarities between collected points optimally and conditioning on the observations yields a stochastic function approximation, i.e. a posterior mean (an approximation of the function) and a posterior variance (the uncertainty). We adopted an anisotropic kernel so that we can handle different correlation length along different directions of the parameter space (f_A, α, and Γ) as described in ESI Equation S1. This is critical in our case, since the physical meaning of the different parameter space axes are very different (and there is no reason for correlation lengths in these disparate directions to be the same). The parameter space in this study exhibits symmetries which originate from the selected definitions. In particular, $M(f_A, \alpha, \Gamma) = M(1 - f_A, -\alpha, 1 - \Gamma)$. For example, a BCP chain with $f_A = 0.25$ should be identical in behavior to one with $f_A = 0.75$, provided the energetics of the A and B blocks are swapped and the substrate energy also inverted. These symmetries are known at the outset and were implemented in the kernel, resulting in ESI Equation S2.[73] Since the GP kernel embodies this symmetry, collection of a data point at a given position (f_A, α, Γ) immediately propagates information to the corresponding symmetric point $(1 - f_A, -\alpha, 1 - \Gamma)$. This reduces the uncertainty in unobserved regions of the domain which leads to significant efficiency gains in data collection. As previously described, the surrogate model obtained from GPR is used for AE, where points are selected by maximizing the data acquisition function. The data acquisition function was constructed to select points along the boundary between vertical and non-vertical morphology; in particular by targeting $f_V = 0.8$ (ESI Equation S3), while also maximizing information gain.

Author Contributions

K.G.Y. and S.B. conceived the project. S.B. designed, performed, and analyzed the MD simulations; K.G.Y. supervised the project. M.N.N. developed the autonomous control software, and related methods. K.G.Y. and S.B. interpreted the results. All authors contributed to writing the manuscript.

Conflicts of interest

The authors declare no competing interests.

Acknowledgement

This research was carried out by the Center for Functional Nanomaterials, which is a U.S. DOE Office of Science Facility, at Brookhaven National Laboratory under Contract No. DE-SC0012704. This work was partially supported by the Laboratory Directed Research and Development program at Brookhaven National Laboratory, and used computational resources managed by the Scientific Data and Computing Center, a component of the Computational Science Initiative, at Brookhaven National Laboratory. Development of autonomous methods was partly funded through the Center for Advanced Mathematics for Energy Research Applications (CAMERA), which is jointly funded by the Advanced Scientific Computing Research (ASCR) and Basic Energy Sciences (BES) within the Department of Energy's Office of Science, under US Department of Energy contract no. DE-AC02-05CH11231.

Notes and references

1 F. S. Bates and G. H. Fredrickson, *Annual Review of Physical Chemistry*, 1990, **41**, 525–557.
2 F. S. Bates and G. H. Fredrickson, *Physics Today*, 1999, **52**, 32–38.
3 M. J. Fasolka and A. M. Mayes, *Annual Review of Materials Research*, 2001, **31**, 323–355.
4 Y. Mai and A. Eisenberg, *Chemical Society Reviews*, 2012, **41**, 5969.
5 G. S. Doerk and K. G. Yager, *Molecular Systems Design & Engineering*, 2017, **2**, 518–538.
6 M. Luo and T. H. Epps, *Macromolecules*, 2013, **46**, 7567–7579.
7 W. I. Park, S. Tong, Y. Liu, I. W. Jung, A. Roelofs and S. Hong, *Nanoscale*, 2014, **6**, 15216–15221.
8 S. V. Roth, G. Santoro, J. F. H. Risch, S. Yu, M. Schwartzkopf, T. Boese, R. Döhrmann, P. Zhang, B. Besner, P. Bremer, D. Rukser, M. A. Rübhausen, N. J. Terrill, P. A. Staniec, Y. Yao, E. Metwalli and P. Müller-Buschbaum, *ACS Applied Materials & Interfaces*, 2015, **7**, 12470–12477.
9 A. Rahman, P. W. Majewski, G. Doerk, C. T. Black and K. G. Yager, *Nature Communications*, 2016, **7**, 13988.
10 T. Thurn-Albrecht, J. Schotter, G. A. Kastle, N. Emley, T. Shibauchi, L. Krusin-Elbaum, K. Guarini, C. T. Black, M. T. Tuominen and T. P. Russell, *Science*, 2000, **290**, 2126–2129.
11 T. Pietsch, P. Müller-Buschbaum, B. Mahltig and A. Fahmi, *ACS Applied Materials & Interfaces*, 2015, **7**, 12440–12449.
12 P. W. Majewski, A. Rahman, C. T. Black and K. G. Yager, *Nature Communications*, 2015, **6**, 7448.
13 A. Rahman, A. Ashraf, H. Xin, X. Tong, P. Sutter, M. D. Eisaman and C. T. Black, *Nature Communications*, 2015, **6**, 5963.
14 A. Checco, A. Rahman and C. T. Black, *Advanced Materials*, 2014, **26**, 886–891.
15 Y. Xuan, J. Peng, L. Cui, H. Wang, B. Li and Y. Han, *Macromolecules*, 2004, **37**, 7301–7307.
16 J. Bang, S. H. Kim, E. Drockenmuller, M. J. Misner, T. P. Russell and C. J. Hawker, *Journal of the American Chemical Society*, 2006, **128**, 7622–7629.
17 V. Khanna, E. W. Cochran, A. Hexemer, G. E. Stein, G. H. Fredrickson, E. J. Kramer, X. Li, J. Wang and S. F. Hahn, *Macromolecules*, 2006, **39**, 9346–9356.
18 M. W. Matsen, *Macromolecules*, 2010, **43**, 1671–1674.
19 T. Vu, N. Mahadevapuram, G. M. Perera and G. E. Stein, *Macromolecules*, 2011, **44**, 6121–6127.
20 S. Jang, K. Lee, H. C. Moon, J. Kwak, J. Park, G. Jeon, W. B. Lee and J. K. Kim, *Advanced Functional Materials*, 2015, **25**, 5414–5419.
21 T.-Y. Lo, A. Dehghan, P. Georgopanos, A. Avgeropoulos, A.-C. Shi and R.-M. Ho, *Macromolecules*, 2016, **49**, 624–633.

22 U. Jeong, D. Ryu, D. Kho, J. Kim, J. Goldbach, D. Kim and T. Russell, *Advanced Materials*, 2004, **16**, 533–536.
23 K. Toth, S. Bae, C. O. Osuji, K. G. Yager and G. S. Doerk, *Macromolecules*, 2021, **54**, 7970–7986.
24 K. G. Yager, B. C. Berry, K. Page, D. Patton, A. Karim and E. J. Amis, *Soft Matter*, 2009, **5**, 622–628.
25 X. M. Yang, R. D. Peters, P. F. Nealey, H. H. Solak and F. Cerrina, *Macromolecules*, 2000, **33**, 9575–9582.
26 S. Ouk Kim, H. H. Solak, M. P. Stoykovich, N. J. Ferrier, J. J. de Pablo and P. F. Nealey, *Nature*, 2003, **424**, 411–414.
27 G. Singh, K. G. Yager, D.-M. Smilgies, M. M. Kulkarni, D. G. Bucknall and A. Karim, *Macromolecules*, 2012, **45**, 7107–7117.
28 P. W. Majewski and K. G. Yager, *Soft Matter*, 2016, **12**, 281–294.
29 H. S. Wang, K. H. Kim and J. Bang, *Macromolecular Rapid Communications*, 2019, **40**, 1800728.
30 P. Mansky, T. P. Russell, C. J. Hawker, M. Pitsikalis and J. Mays, *Macromolecules*, 1997, **30**, 6810–6813.
31 E. Huang, T. P. Russell, C. Harrison and P. M. Chaikin, *Macromolecules*, 1998, **31**, 10.
32 D. Y. Ryu, *Science*, 2005, **308**, 236–239.
33 E. Han, I. In, S.-M. Park, Y.-H. La, Y. Wang, P. Nealey and P. Gopalan, *Advanced Materials*, 2007, **19**, 4448–4452.
34 C. Forrey, K. G. Yager and S. P. Broadaway, *ACS Nano*, 2011, **5**, 2895–2907.
35 G. E. Stein, T. S. Laws and R. Verduzco, *Macromolecules*, 2019, **52**, 4787–4802.
36 E. Han, K. O. Stuen, Y.-H. La, P. F. Nealey and P. Gopalan, *Macromolecules*, 2008, **41**, 9090–9097.
37 S. Ham, C. Shin, E. Kim, D. Y. Ryu, U. Jeong, T. P. Russell and C. J. Hawker, *Macromolecules*, 2008, **41**, 6431–6437.
38 P. Mansky, T. P. Russell, C. J. Hawker, J. Mays, D. C. Cook and S. K. Satija, *Physical Review Letters*, 1997, **79**, 237–240.
39 J. Brandrup, E. H. Immergut and E. A. Grulke, *Polymer Handbook*, John Wiley, 1999.
40 E. Han, K. O. Stuen, M. Leolukman, C.-C. Liu, P. F. Nealey and P. Gopalan, *Macromolecules*, 2009, **42**, 4896–4901.
41 K. G. Yager, E. Lai and C. T. Black, *ACS Nano*, 2014, **8**, 10582–10588.
42 J. Chai, D. Wang, X. Fan and J. M. Buriak, *Nature Nanotechnology*, 2007, **2**, 500–506.
43 H. M. Nguyen, A. V. Mader, S. De and J. Vapaavuori, *Nanoscale Advances*, 2021, **3**, 4996–5007.
44 Y. S. Jung and C. A. Ross, *Nano Letters*, 2007, **7**, 2046–2050.
45 I. Bita, J. K. W. Yang, Y. S. Jung, C. A. Ross, E. L. Thomas and K. K. Berggren, *Science*, 2008, **321**, 939–943.
46 K. Kremer and G. S. Grest, *The Journal of Chemical Physics*, 1990, **92**, 5057–5086.
47 F. M. Capaldi, M. C. Boyce and G. C. Rutledge, *Physical Review Letters*, 2002, **89**, 175505.
48 S. Bae, O. Galant, C. E. Diesendruck and M. N. Silberstein, *Macromolecules*, 2018, **51**, 7160–7168.
49 G. S. Grest, M. Lacasse, K. Kremer and A. M. Gupta, *The Journal of Chemical Physics*, 1996, **105**, 10583–10594.
50 A. Knoll, A. Horvat, K. S. Lyakhova, G. Krausch, G. J. A. Sevink, A. V. Zvelindovsky and R. Magerle, *Physical Review Letters*, 2002, **89**, 035501.
51 J. H. Ryu, H. S. Wee and W. B. Lee, *Physical Review E*, 2016, **94**, 032501.
52 Y. Seo, K.-H. Shen, J. R. Brown and L. M. Hall, *Journal of the American Chemical Society*, 2019, **141**, 18455–18466.
53 J. N. Albert and T. H. Epps, *Materials Today*, 2010, **13**, 24–33.
54 P. W. Majewski and K. G. Yager, *Journal of Physics: Condensed Matter*, 2016, **28**, 403002.
55 C. T. Black, C. Forrey and K. G. Yager, *Soft Matter*, 2017, **13**, 3275–3283.
56 M. M. Noack, P. H. Zwart, D. M. Ushizima, M. Fukuto, K. G. Yager, K. C. Elbert, C. B. Murray, A. Stein, G. S. Doerk, E. H. R. Tsai, R. Li, G. Freychet, M. Zhernenkov, H.-Y. N. Holman, S. Lee, L. Chen, E. Rotenberg, T. Weber, Y. L. Goc, M. Boehm, P. Steffens, P. Mutti and J. A. Sethian, *Nature Reviews Physics*, 2021, **3**, 685–697.
57 S. Bae and K. G. Yager, *ACS Nano*, 2022, **16**, 17107–17115.
58 T. P. Russell, A. Menelle, S. H. Anastasiadis, S. K. Satija and C. F. Majkrzak, *Macromolecules*, 1991, **24**, 6263–6269.
59 M. Maaloum, D. Ausserre, D. Chatenay and Y. Gallot, *Physical Review Letters*, 1993, **70**, 2577–2580.
60 S. Joly, D. Ausserré, G. Brotons and Y. Gallot, *The European Physical Journal E*, 2002, **8**, 355–363.
61 P. Mahmoudi and M. W. Matsen, *The European Physical Journal E*, 2017, **40**, 85.
62 S. T. Russell, S. Bae, A. Subramanian, N. Tiwale, G. Doerk, C.-Y. Nam, M. Fukuto and K. G. Yager, *Nature Communications*, 2022, **13**, 6947.
63 M. N. Basutkar, S. Samant, J. Strzalka, K. G. Yager, G. Singh and A. Karim, *Nano Letters*, 2017, **17**, 7814–7823.
64 R. D. Groot and T. J. Madden, *The Journal of Chemical Physics*, 1998, **108**, 8713–8724.
65 A. J. Schultz, C. K. Hall and J. Genzer, *The Journal of Chemical Physics*, 2002, **117**, 10329–10338.
66 C.-I. Huang and Y.-C. Lin, *Macromolecular Rapid Communications*, 2007, **28**, 1634–1639.
67 K. G. Yager, C. Forrey, G. Singh, S. K. Satija, K. A. Page, D. L. Patton, J. F. Douglas, R. L. Jones and A. Karim, *Soft Matter*, 2015, **11**, 5154–5167.
68 S. Plimpton, *Journal of Computational Physics*, 1995, **117**, 1–19.
69 W. Humphrey, A. Dalke and K. Schulten, *Journal of Molecular Graphics*, 1996, **14**, 33–38.
70 M. M. Noack, K. G. Yager, M. Fukuto, G. S. Doerk, R. Li and J. A. Sethian, *Scientific Reports*, 2019, **9**, 11809.
71 M. M. Noack, G. S. Doerk, R. Li, M. Fukuto and K. G. Yager, *Scientific Reports*, 2020, **10**, 1325.
72 M. M. Noack, G. S. Doerk, R. Li, J. K. Streit, R. A. Vaia, K. G. Yager and M. Fukuto, *Scientific Reports*, 2020, **10**, 17663.
73 M. M. Noack and J. A. Sethian, *Communications in Applied Mathematics and Computational Science*, 2021, **17**, 131–156.